QUANTUM OPTICS

Photoelectrical imaging and coherent spin-state readout of single nitrogen-vacancy centers in diamond

Petr Siyushev[1,2]*†, Milos Nesladek[3,4,5]*†, Emilie Bourgeois[3,4], Michal Gulka[3,4,5], Jaroslav Hruby[3,4], Takashi Yamamoto[3,4]‡, Michael Trupke[6], Tokuyuki Teraji[7], Junichi Isoya[8]§, Fedor Jelezko[1]

Nitrogen-vacancy (NV) centers in diamond have become an important instrument for quantum sensing and quantum information science. However, the readout of NV spin state requires bulky optical setups, limiting fabrication of miniaturized compact devices for practical use. Here we realized photoelectrical detection of magnetic resonance as well as Rabi oscillations on a single-defect level. Furthermore, photoelectrical imaging of individual NV centers at room temperature was demonstrated, surpassing conventional optical readout methods by providing high imaging contrast and signal-to-noise ratio. These results pave the way toward fully integrated quantum diamond devices.

Electrical readout is a convenient way to measure the spin state of a qubit, and it has been successfully applied to semiconductor systems such as quantum dots (*1*, *2*), phosphorous donors (*3*), and erbium ions (*4*) in silicon. However, all these examples require low temperature. In experiments with nitrogen-vacancy (NV) centers—which are prominent candidates for magnetic field sensing (*5*, *6*), nanoscale nuclear magnetic resonance (*7*), and quantum information processing (*8*, *9*)—optical methods are used for defects visualization and spin-state readout. Recently, photoelectrical detection of magnetic resonance (PDMR) (*10*), photoelectrical readout of electron (*11*, *12*) and nuclear (*13*) spins have been demonstrated on ensembles of NV centers under ambient conditions. However, the fundamentals of quantum technologies rest on the coherent driving and readout of single qubits. Ensemble experiments demonstrated a strong background signal produced by nitrogen impurities that provide additional contribution to the photoinduced current. For this reason, the step toward single NV center detection has been a challenging task.

The idea of photoelectrical detection is based on intrinsic charge dynamics occurring under continuous light illumination (*14*, *15*). The excited state of the negatively charged NV center (NV^-) lies close enough to the conduction band, so that the electron promoted to the excited state can either radiatively decay or undergo further excitation to the conduction band (Fig. 1A). There, it can freely travel under an applied electric field and finally be detected. However, photoionization alters the charge of the defect and thus its electronic level structure. The ground state of the neutral NV center (NV^0) is shifted toward the valence band, enabling recovery of the negative charge state. The only requirement for dynamical cycling between these two counterparts is that the photon excitation energy should be greater than the energy of the zero-phonon line of the NV^0 center (*15*). Within one cycle, two charge carriers are produced: one electron during ionization and one hole during NV^- recovery. This dynamical charge circulation enables the photoelectrical readout of NV centers, unlike other defects.

For our experiments, two types of diamond were used. The first type (represented by two ultrapure diamonds called sample a and sample b below) was undoped, ultrapure, chemical

[1]Institute for Quantum Optics and IQST, Ulm University, Albert-Einstein-Allee 11, D-89081 Ulm, Germany. [2]Corporate Research and Technology, Carl Zeiss AG, Carl-Zeiss-Strasse 22, 73447 Oberkochen, Germany. [3]IMOMEC division, IMEC, Wetenschapspark 1, B-3590 Diepenbeek, Belgium. [4]Institute for Materials Research (IMO), Hasselt University, Wetenschapspark 1, B-3590 Diepenbeek, Belgium. [5]Department of Biomedical Technology, Faculty of Biomedical Engineering, Czech Technical University in Prague, Sítna sq. 3105, 27201 Kladno, Czech Republic. [6]Vienna Center for Quantum Science and Technology (VCQ), Faculty of Physics, University of Vienna, Boltzmanngasse 5, A-1090 Vienna, Austria. [7]National Institute for Materials Science, 1-1 Namiki, Tsukuba, Ibaraki 305-0044, Japan. [8]Research Center for Knowledge Communities, University of Tsukuba, Tsukuba, Ibaraki 305-8550, Japan.
*These authors contributed equally to this work.
†Corresponding author. Email: petr.siyushev@uni-ulm.de (P.S.); milos.nesladek@uhasselt.be (M.N.) ‡Present address: QuTech, Delft University of Technology, P.O. Box 5046, 2600 GA Delft, Netherlands. §Present address: Faculty of Pure and Applied Sciences, University of Tsukuba, Tsukuba, Ibaraki 305-8573, Japan.

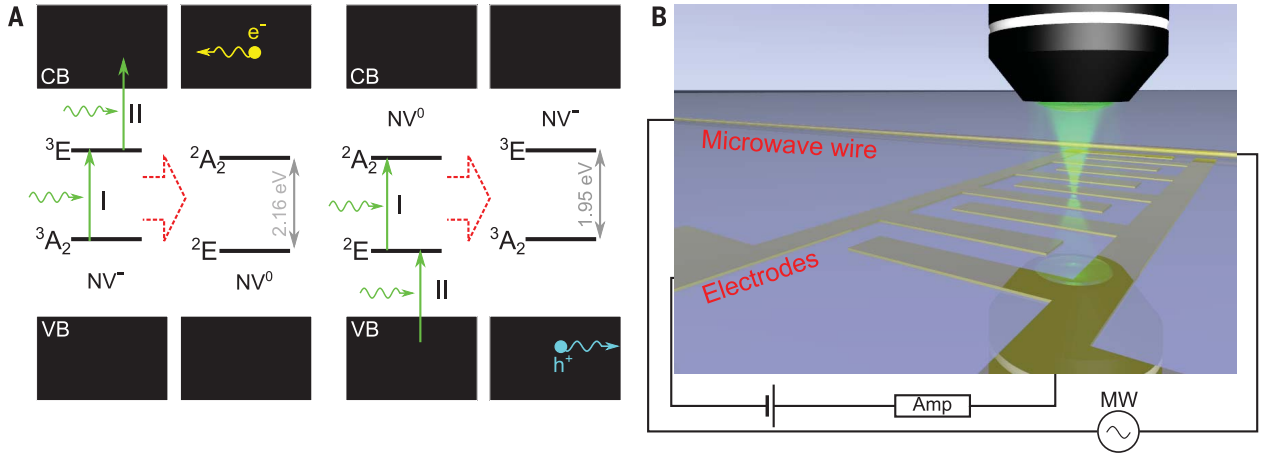

Fig. 1. Schematic representation of the experiment. (**A**) Simplified representation of the charge-carrier generation within one cycle of NV^- ionization and recovery. First, two photons produce one free electron in the conduction band (CB) and leave defects in the neutral charge state. Second, two photons convert the neutral charge state back to NV^-, while a free hole remains in the valence band (VB). I and II indicate first and second transitions of the electrons. e and h represent electron and hole, respectively. (**B**) Configuration of the single-center photoelectrical imaging setup. Coplanar and electrodes deposited on the diamond surface are connected in series with a power supply and current amplifier (Amp). The microscope objective lens scans over the sample surface, while a microwave (MW) field can be applied via a 50-μm-thick wire placed near the electrodes.

vapor–deposited (CVD) diamond with a nitrogen concentration below 0.15 parts per billion and which contained only native NV centers. The second type was a diamond produced by nitrogen doping during chemical vapor–deposition growth (sample c). This sample contained engineered shallow NV centers, which is relevant for sensing applications. Subsequently, this diamond was polished under a small angle to form a gradient of shallow NV centers along the sample surface. Titanium electrodes coated with either gold or aluminum were produced on the surface by photolithography (see the supplementary materials for sample preparation). The distance from the NV centers to the electrodes varies from 1 to 20 μm.

We started by characterizing an area between the electrodes of the ultrapure sample a in confocal arrangement (Fig. 1B) and found a few sparse NV centers at a depth of ~16 μm. An example optical image is shown in Fig. 2A. The photon autocorrelation function was recorded on several defects. An antibunching dip below 0.5 at zero delay clearly indicates single defects (Fig. 2B). The same area was scanned by a focused laser beam while applying a voltage across the electrodes, and the electrical current flowing between electrodes was recorded as a function of illuminated point coordinates (Fig. 2C).

To characterize the photocurrent produced by a single center, we performed the following steps. First, the voltage across the electrodes was set to the point at which current saturates. Further increase of the voltage is unreasonable owing to contact leakage (see the supplementary materials). Second, a series of scans with electrical readout were obtained for different values of laser power. In each image, the spot corresponding to the NV center is fitted by a Gaussian function (Fig. 2D) and the amplitude and background values extracted. They are plotted as a function of laser power in Fig. 2F. The photocurrent originating from a single NV center has a contribution from both types of charge carriers: electrons and holes. Under green excitation, their generation is a two-photon process

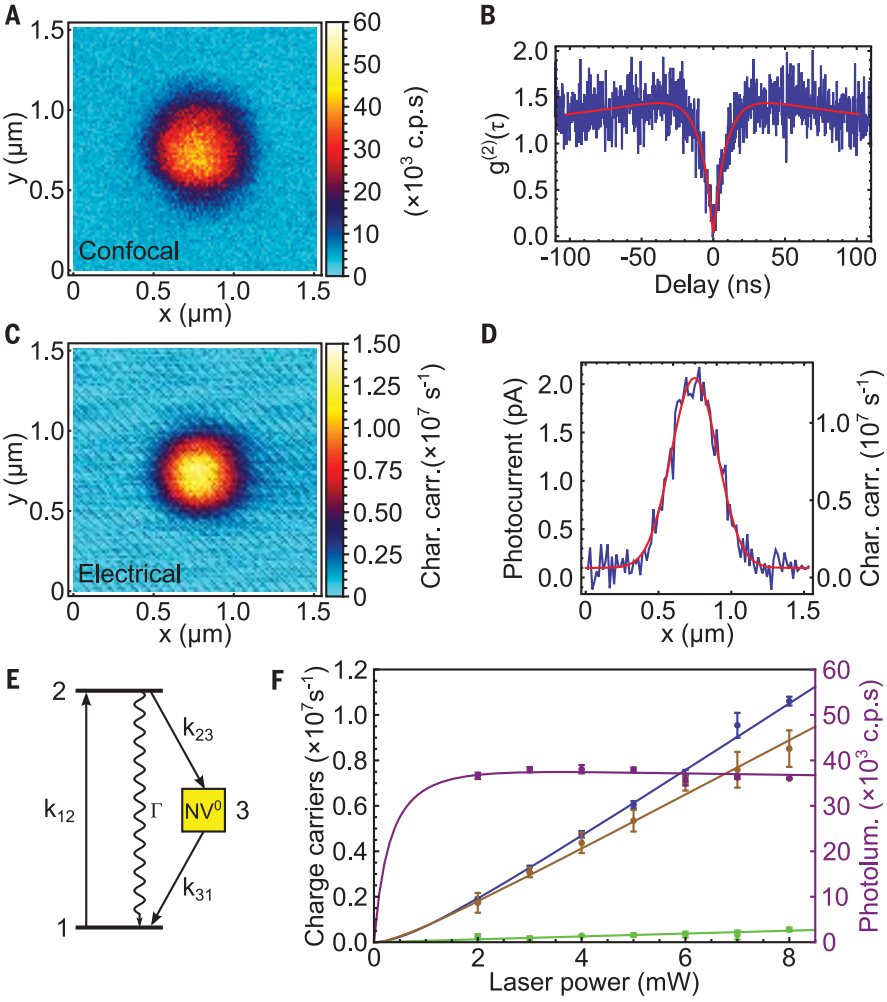

Fig. 2. Photoelectrical imaging. (**A**) Confocal image of the 1.5-μm–by–1.5-μm area between electrodes. (**B**) Photon autocorrelation function [$g^{(2)}(\tau)$] obtained from the spot in the image (A) indicates that a single NV center is addressed. (**C**) Photoelectrical image of the same area recorded at 9 mW of laser excitation power and applied voltage of 80 V. (**D**) Cross-section through the middle of the image (C), fitted with a Gaussian function. (**E**) Three-level model used to estimate the number of charge carriers generated under constant laser illumination. The model does not differentiate between the metastable state and another charge state. (**F**) Comparison of the number of charge carriers generated per second obtained from photocurrent measurements (blue data points) and from antibunching (brown data points). Both curves coincide well at low power. The deviation that occurs for increased powers results from the increasing fit error of antibunching curves. Green data points show background dependence. Purple data points represent the number of detected photons per second as a function of laser power. The solid purple curve is the fit to the data by the same model used for estimation of charge-carrier generation rate. The only free fit parameter is the photon detection efficiency (0.16% from the fit).

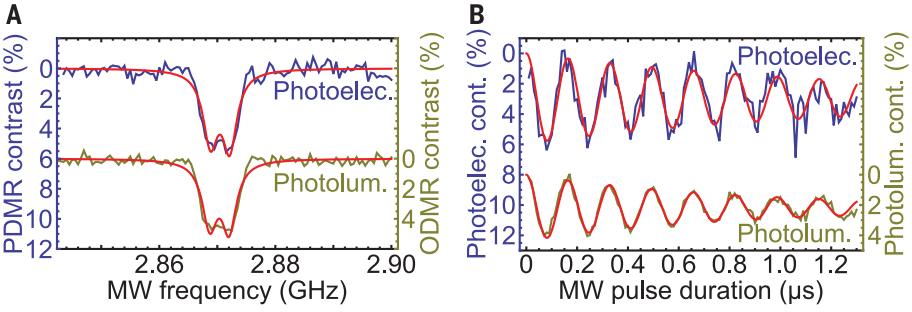

Fig. 3. Photoelectrical readout of a single electron spin. (**A**) Contrast of the PDMR (4.6%) and optically detected magnetic resonance (ODMR) (4.3%) signals simultaneously measured on a single NV center. The experimental data were corrected for a linear drift and were fitted using a double Lorentzian function (red line). (**B**) Contrast of the photoelectrically (6%) and optically (4%) detected Rabi oscillations. The red lines correspond to a fit of the experimental data.

with a scaling that can be described by the function (*15*) $\alpha\beta I^2/(1 + \beta I)$, where I is the laser intensity and α and β are constants. At the low power limit, the curve has a quadratic growth, indicating a two-photon process. At higher powers, the curve becomes linear, because the first transition saturates and the population of the intermediate level changes weakly. The background photocurrent remains small for the entire range of measured powers. Its linear growth suggests that the background originates from other defects, such as substitutional nitrogen, in the diamond crystal.

To make a rough estimation of the charge-carrier generation rate, we used a simple method based on photon autocorrelation function measurements. The second-order autocorrelation function exhibits an antibunching dip at zero-delay time and bunching wings at finite delays. Whereas antibunching is a signature of a single photon source, bunching shoulders characterize the internal dynamics of the system and indicate the presence of a shelving state, where the population is trapped for some time. Previously, this trapping state was typically associated with metastable states of the NV^- center (*16*), although it was known that the bunching time is power-dependent (*17*). This fact contradicts the nonradiative nature of the relaxation dynamics from the excited state to the metastable state. Photoionization is another mechanism responsible for the excited-state depopulation, which, indeed, depends on the laser power and has not been taken into account previously. Hence, at low laser intensities, shelving to the metastable state defines bunching, whereas with an increase in the laser intensity, photoionization-induced "shelving" into the neutral charge state starts to play the primary role. This assumption is also supported by the power-dependent deshelving rate. Therefore, we can estimate the number of electrons and holes produced during illumination of the NV center using a simple three-level system depicted in Fig. 2E. Using this model, we fit the photon autocorrelation function to extract the rates of photoionization and negative-charge-state recovery (see the supplementary materials). The number of electrons (holes) generated per second is found as a product of the ionization k_{23} (recovery k_{31}) rate with ρ_2 (ρ_3)—the steady-state population of the level from which the transition occurs. The photocurrent is thus defined as $I_{pc} = (k_{23}\rho_2 + k_{31}\rho_3)e$, where e is the elementary charge of an electron. Comparison of the charge carrier's generation rate extracted from photocurrent measurements (blue) and from the photon autocorrelation (brown) is depicted in Fig. 2F. The data are in good agreement at low laser powers, whereas a small deviation is observed at higher powers. This mismatch arises from an increasing error for the rate extraction at high laser powers. This is due to narrowing of the antibunching dip and to the reduction of its contrast caused by timing jitter of the avalanche photodiodes. The purple data points in Fig. 2F show the number of extracted photons from the same NV center that reaches its maximum at about 3.8×10^4 counts per second (c.p.s.) and then slightly decreases owing to reduction of the population ρ_2 caused by ionization. A fit to the data was done by $\eta\Gamma\rho_2$ (where Γ is the radiative decay rate of the excited state) with the parameters obtained from photon autocorrelation measurements, so that only the detection efficiency η was used as a variable fit parameter. Whereas the saturation behavior fundamentally limits the number of detectable photons, linear scaling of the photocurrent allows production of more charge carriers for detection by a simple increase in the laser excitation power. The same center yields about 1.1×10^7 charge carriers per second at a laser power of 8 mW.

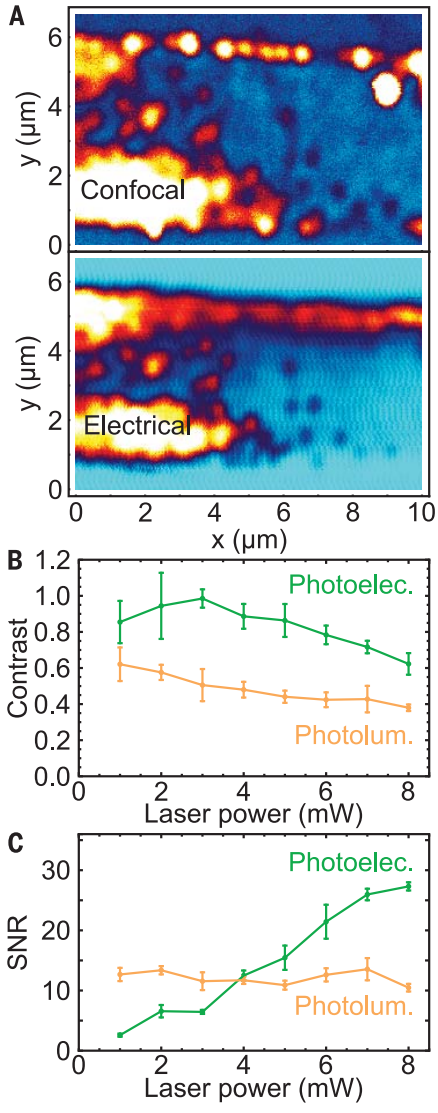

Fig. 4. Photoelectrical detection of engineered NV centers. (**A**) Confocal and photoelectrical images of the same area. (**B**) Contrast of the image as a function of the laser power for electrical and optical signals. The contrast of the electrical image (green data) reaches 98% between 2 and 4 mW, whereas optical contrast (orange data) constantly decreases from a value of 62%. (**C**) SNR of the image as a function of laser power. Electrical SNR (green data) is limited by cross-talk noise and increases with the laser power. Optical SNR (orange data) is limited by photon shot noise and slowly decreases owing to growing background.

With the ability to detect and image the photocurrent resulting from the ionization of a single NV center, we demonstrate PDMR as well as electrical readout of a coherently prepared electron spin state. For this experiment, we used sample b, in which native single NV centers could be found at a depth of ~2 μm below the diamond surface. To avoid limitations imposed by the high laser power onto the PDMR contrast (see the supplementary materials), not only Rabi but also PDMR measurements were performed in a pulsed mode. Figure 3 shows a comparison of the electrically read out magnetic resonance and Rabi oscillations of the NV center spin with simultaneously obtained optical signals. In the conditions considered here (see the supplementary materials), the contrast of the signals obtained by photoelectrical detection is comparable to or even exceeds the optical one.

To explore photoelectrical imaging, we utilized the diamond sample c with a variable density of NV centers situated within a depth of a few nanometers below the surface. Simultaneously obtained images of confocal and electrical scans are depicted in Fig. 4A. The area shows bright clusters of NV defects as well as single centers verified by antibunching measurements. Compared to electronic grade diamond, this sample presents a lower-lying layer of NV centers in the Ib substrate. The CVD layer also contains a higher concentration of nitrogen impurities than NV centers (conversion ratio of nitrogen into NV defects of only 100 to 1) (*18*). These different factors lead to a background photocurrent that constrains the imaging contrast. By performing measurements similar to those performed on sample a, we found that this background restricts the optimal laser power to between 2 and 4 mW, where the imaging contrast reaches its maximum of 98% (green data points in Fig. 4B). The contrast of electrical imaging always remains better than that of optical imaging. The latter does not exceed 62% (orange data points), owing to high background fluorescence from the NV layer beneath that cannot be completely discriminated by the pinhole. The background fluorescence also reduces the optical signal-to-noise ratio (SNR) (orange data points in Fig. 4C). Photoelectrical SNR (green data points) is limited by parasitic cross-talk, mainly 50-Hz technical noise of the electrical network, clearly visible in Fig. 4A as a set of periodical lines, which we could not completely suppress. The technical noise can be further improved by a proper design of the detection circuit, and the electron shot noise limit can ideally be reached.

The results presented here demonstrate the high potential of photoelectrical detection of coherently driven single NV centers, opening possibilities for simple and reliable implementation of diamond quantum devices that are

compatible with technology used in the electronics industry. This method offers advantages compared to conventional optical techniques, such as the high charge-carrier detection rate, which does not saturate with the applied optical power, and the high signal contrast even in circumstances where confocal detection cannot provide it. We anticipate that electrical readout will boost fabrication of compact magnetometers and recently established lab-on-a-chip devices (*19*) for biology and medicine. Because this technique is capable of single charge-carrier generation on demand, it can be applied in quantum metrology as a standard for the electrical unit ampere (*20*). Moreover, this technique can be potentially transferred to new defects in diamond (*21*–*23*) as well as to other wide-bandgap semiconductors (*24*), where defects can be ionized.

REFERENCES AND NOTES

1. J. M. Elzerman *et al.*, *Nature* **430**, 431–435 (2004).
2. J. M. Nichol *et al.*, *npj Quantum Inf.* **3**, 3 (2017).
3. J. J. Pla *et al.*, *Nature* **489**, 541–545 (2012).
4. C. Yin *et al.*, *Nature* **497**, 91–94 (2013).
5. J. M. Taylor *et al.*, *Nat. Phys.* **4**, 810–816 (2008).
6. L. Rondin *et al.*, *Rep. Prog. Phys.* **77**, 056503 (2014).
7. H. J. Mamin *et al.*, *Science* **339**, 557–560 (2013).
8. W. Pfaff *et al.*, *Science* **345**, 532–535 (2014).
9. E. Togan *et al.*, *Nature* **466**, 730–734 (2010).
10. E. Bourgeois *et al.*, *Nat. Commun.* **6**, 8577 (2015).
11. M. Gulka *et al.*, *Phys. Rev. Appl.* **7**, 044032 (2017).
12. F. M. Hrubesch, G. Braunbeck, M. Stutzmann, F. Reinhard, M. S. Brandt, *Phys. Rev. Lett.* **118**, 037601 (2017).
13. H. Morishita *et al.*, arXiv:1803.01161 [cond-mat.mes-hall] (3 March 2018).
14. N. Aslam, G. Waldherr, P. Neumann, F. Jelezko, J. Wrachtrup, *New J. Phys.* **15**, 013064 (2013).
15. P. Siyushev *et al.*, *Phys. Rev. Lett.* **110**, 167402 (2013).
16. M. Berthel *et al.*, *Phys. Rev. B* **91**, 035308 (2015).
17. A. Beveratos, R. Brouri, J.-P. Poizat, P. Grangier, arXiv: quant-ph/0010044 [quant-ph] (11 October 2000).
18. A. M. Edmonds *et al.*, *Phys. Rev. B* **86**, 035201 (2012).
19. D. Figeys, D. Pinto, *Anal. Chem.* **72**, 330A–335A (2000).
20. L. Fricke *et al.*, *Phys. Rev. Lett.* **112**, 226803 (2014).
21. E. Londero, E. Bourgeois, M. Nesladek, A. Gali, *Phys. Rev. B* **97**, 241202 (2018).
22. C. Hepp *et al.*, *Phys. Rev. Lett.* **112**, 036405 (2014).
23. P. Siyushev *et al.*, *Phys. Rev. B* **96**, 081201 (2017).
24. P. Siyushev *et al.*, *Nat. Commun.* **5**, 3895 (2014).

ACKNOWLEDGMENTS

P.S. acknowledges discussions with A. Ermakova (Max Planck Institute for Polymer Research). M.N. acknowledges discussions with A. Gali (Wigner Research Centre for Physics).

Funding: M.N., M.T., and F.J. acknowledge project R-8843 Q-Magine of the QUANTERA. M.N. acknowledges support from the FWO projects S004018N DIAQUANT and G0E7417N. M.N. and F.J. acknowledge support from EU ASTERIQS (820394). F.J. acknowledges support from the DFG (JE 290/18-1 and SFB 1279), BMBF (13N14438, 16KIS0832, and 13N14810), ERC (BioQ 319130), T.T. acknowledges support of Grants-in-Aid for Scientific Research from the Ministry of Education, Culture, Sports, Science, and Technology, Japan (15H03980, 26220903, and 278 16H06326) and Japan Science and Technology Agency (JST) CREST (JPMJCR1773). VW Stiftung (93432), and Landesstiftung (BW-INT SF III-042). **Author contributions:** P.S., M.N., and E.B. designed the experiments. P.S., M.N., E.B., M.G., and J.H. conducted the experiments. T.T. and J.I. fabricated and T.Y. characterized the δ-doped sample. M.T. prepared electrodes on sample a. P.S. analyzed the data. F.J. and M.N. supervised the project. All authors discussed the results and commented on the manuscript. **Competing interests:** P.S. has paid activity at Carl Zeiss AG. **Data and materials availability:** All data are available in the manuscript or the supplementary materials.

SUPPLEMENTARY MATERIALS

www.sciencemag.org/content/363/6428/728/suppl/DC1
Materials and Methods
Supplementary Text
Figs. S1 to S5
References (*25*–*29*)

31 August 2018; accepted 21 January 2019
10.1126/science.aav2789

Photoelectrical imaging and coherent spin-state readout of single nitrogen-vacancy centers in diamond

Petr Siyushev, Milos Nesladek, Emilie Bourgeois, Michal Gulka, Jaroslav Hruby, Takashi Yamamoto, Michael Trupke, Tokuyuki Teraji, Junichi Isoya and Fedor Jelezko

Science **363** (6428), 728-731.
DOI: 10.1126/science.aav2789

An integrated route to quantum detection

The quantum properties of the nitrogen-vacancy (NV) center defect in diamond are being pursued as building blocks for quantum-enhanced technologies. Addressing and manipulating the defects, however, typically requires bulk optics, which could limit scalability. Siyushev *et al.* developed an on-chip technique in which the NV center is detected optoelectronically. Such a detection and manipulation method offers a route to develop an integrated platform for scalable quantum-based sensing technologies.

Science, this issue p. 728